Fluid driven percolation in barrier rock: experiments and numerical simulation

KY AS MN FW TN OK

Abstract

Underground usage for energy storage or nuclear waste disposal is becoming important. In doing so, barrier rock integrity needs to be ensured. Mechanical integrity of barrier rock is studied both experimentally and numerically.

Nomenclature

$\mathbf{f}$	Traction vector
ψ	Strain energy

1. Introduction

Geomechanical integrity is evaluated.

2. Fluid percolation (hydraulic fracturing) experiments on rock salt

For comparison with numerical models, we used published experiments on pressure driven percolation (hydraulic fracturing) [21]. The experiments were conducted in salt stone to study stress dependent hydraulic fracture propagation.

Cubic samples with 100 mm edge length were prepared with a borehole in the upper middle boundary (Fig. 1(a)). The samples were loaded with with a true-triaxial apparatus and pressurized fluid was injected through a borehole drilled in the middle of the sample to induce hydraulic fracture (Fig. 1(b)). The depth of and the diameter of the hole are 50 mm and 20 mm respectively. The drilled hole was cased off to a depth of 40 mm leaving a 10 mm open section in the bottom for fluid entry to the sample.

Two different stress states were applied to the samples. The first case is a reverse faulting in Adersonian stress state [5] (Fig. 2(a)) and the resulting crack patterns are shown in Figs. 2(a) and 2(b). During injection of the fluid, the flow rate was kept constant and the pressure responses were recorded. Figs. 3(a) and 3(b) show evolution of the pressures.

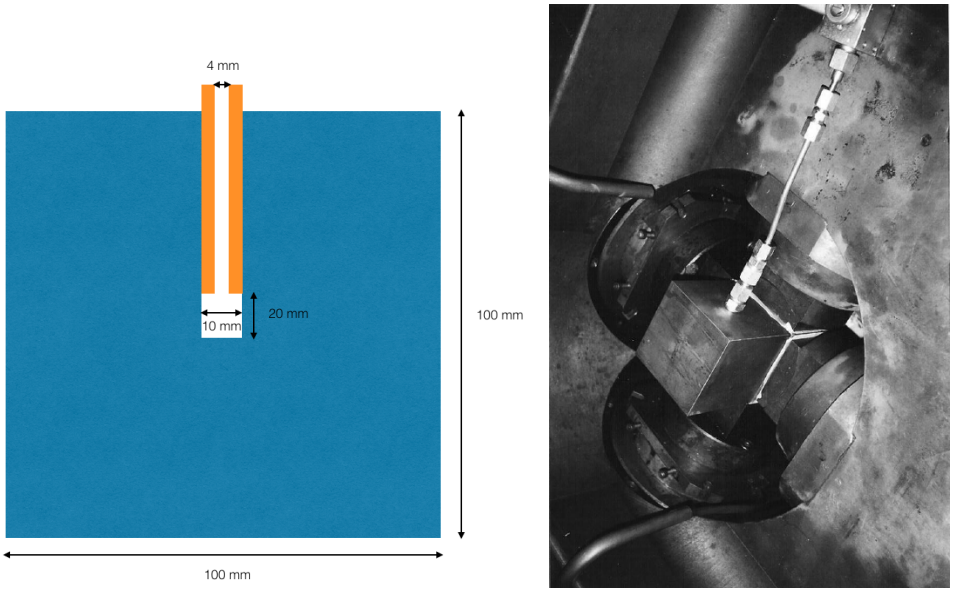

(a) Schematic of the experiment

(b) Configuration inside the true tri-axial apparatus

Figure 1: Pressure-driven fluid percolation experiment in rock salt in [21]

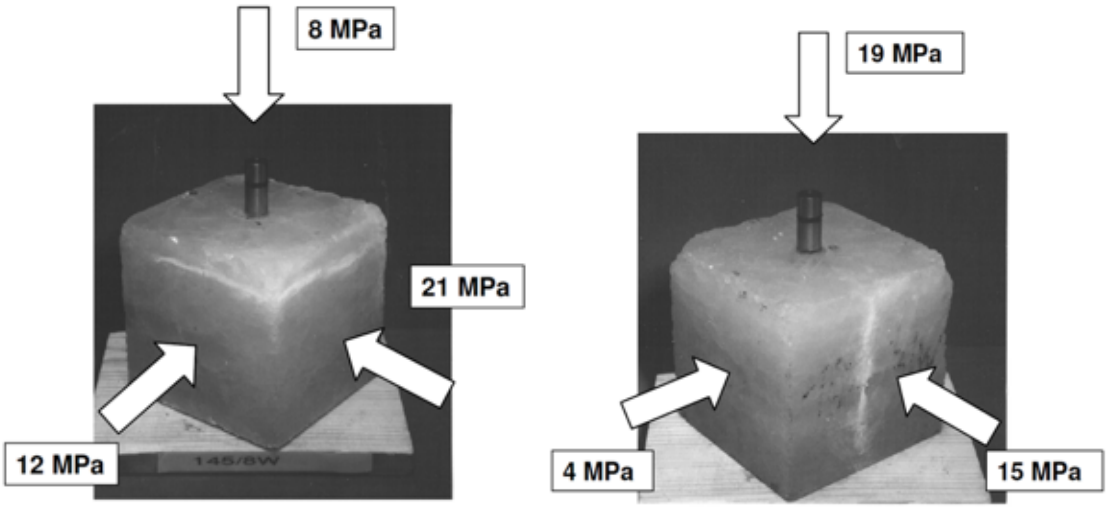

(a) Reverse faulting stress configuration

(b) Normal faulting stress configuration

Figure 2: The confining stress configurations in salt stone [21]

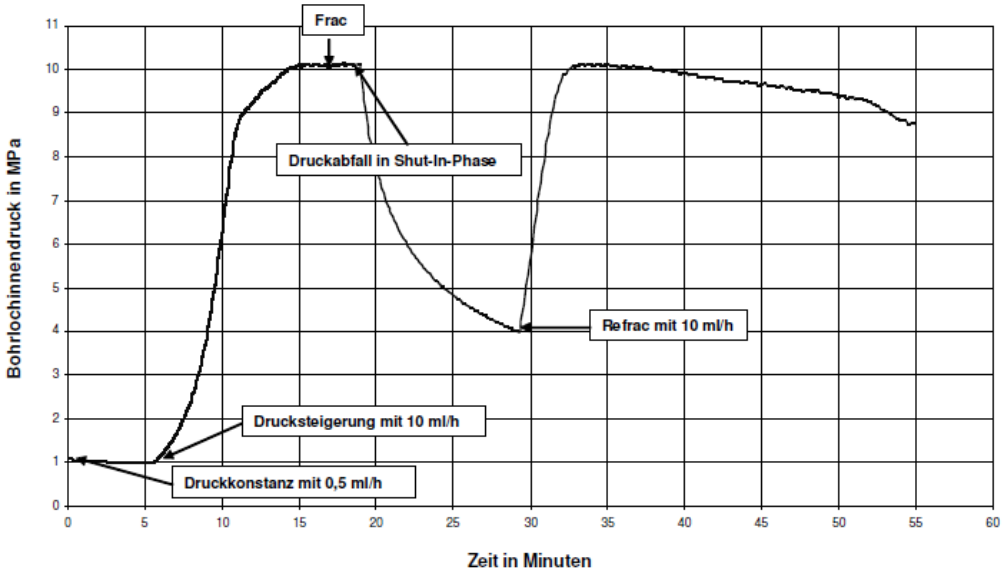

(a) Result from 2(a)

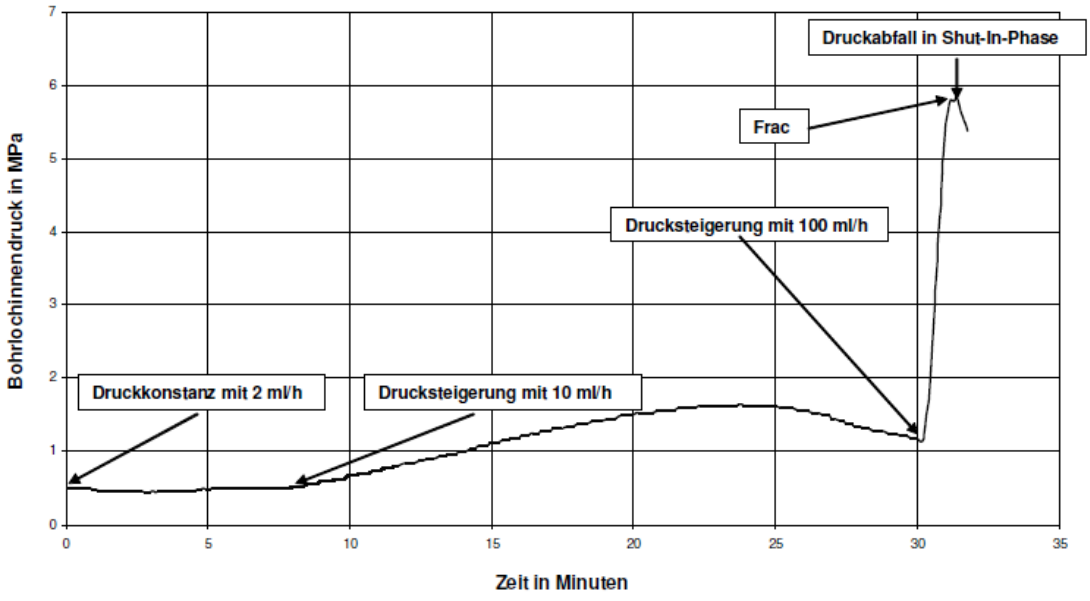

(b) Result from 2(b)

Figure 3: The borehole pressure evolution under constant flow rate sequels [21]

3. Model approach

Static equilibrium in the absence of body forces and continuity of stress under the presence of crack set Γ is given by:

$$\begin{cases} \nabla \cdot \boldsymbol{\sigma}(\mathbf{u}) = \mathbf{0} & \text{in } \Omega \setminus \Gamma, \\ \boldsymbol{\sigma} \cdot \mathbf{n} = \mathbf{t} & \text{on } \partial\Omega_{\mathrm{N}}, \\ \mathbf{u} = \mathbf{u}_0 & \text{on } \partial\Omega_{\mathrm{D}}, \\ \boldsymbol{\sigma}^{\pm} \cdot \mathbf{n}_{\Gamma^{\pm}} = -p\mathbf{n}_{\Gamma^{\pm}} & \text{on } \Gamma^{\pm}. \end{cases} \tag{1}$$

3.1. Discrete element model

3.2. Lattice element model

The application of discrete lattice element in modeling the fracture initiation and propagation in geomaterials is well established [28, 36, 46]. The main advantage of LEM is to model the stress redistribution and concentration upon the fracking process. The application of LEM is extended recently to model the heat transfer in cemented geomaterials [42] as well as granular particles [38]. The thermo-mechanical lattice model based on the integration of the interface element is able to model extension and shrinkage processes during heating and cooling processes [41]. The LEM is also extended to model the foam concrete behavior under dynamic loading [40]. In the recent decade, the dual lattice model to simulate the coupled hydro-mechanical loadings is geomaterials is developed [16]. In these models, the additional mesh grid for transportation of hydraulic flow is considered. The short description of the implemented coupled thermo-hydro-mechanical lattice is given below.

3.2.1. Discretization of the domain

The domain is discretized into a series of Voronoi cells which represent the particle or continuum depending on the domain boundary condition. With the application of the Vectorized random lattice (VRL), the irregularity factor known as the randomness factor (), which varies between 0 and 1 is introduced [33]. When the randomness factor is 0, the generated mesh is regular and when it is equal to 1, it reaches the maximum irregularity for VRL model. Afterward, the Voronoi Tesselation is implemented and the continuum or particle boundaries are defined. The Delaunay Triangulation results in the Voronoi cell connectivity which will be considered as bond lattice elements between each node.

3.2.2. Mechanical lattice model

The mechanical lattice model is based on the assumption of linear elastic fracture mechanics and, where mode I and II fracture mechanisms are considered. The simulation of fracture in LEM is based on the removal of the bond elements between Voronoi cells [37]. The elements strength threshold can be defined based on critical strain energy or fracture toughness for Mode I and II. In a different approach, the strength threshold is defined based on Mohr-Coulombs tension cutoff model [6]. The lattice elements can be represented by a spring (1DOF), Euler-Bernoulli beam (3DOF) or Timoshenko beam elements (4DOF). The regularization of regular lattice models are carried out and a relationship between the continuum and element properties are presented [34, 22]. This regularization is based on the assumption of the fact that the stored strain energy of the continuum should be equal to the stored strain energies in each discretized Voronoi cells.

$$
\begin{aligned}
U_{Cell} &= U_{Continuum} \\
U_{Cell} &= \frac{1}{2}\sum_{b}^{N_b}(F.u)^b \\
U_{Continuum} &= \frac{1}{2}\int_V \sigma.\varepsilon.dV
\end{aligned}
\tag{2}
$$

For a spring element in 2D,

$$
\begin{aligned}
U_{Cell} = \frac{1}{2}\sum_{b}^{N_b}(F.u)^b = \frac{1}{2}\sum_{b=1}^{N_b}(L^2).\alpha'.n_i.n_j.n_k.n_m.\epsilon_{ij}.\varepsilon_{km} \\
U_{Continuum} = \frac{1}{2}\varepsilon.C.\varepsilon
\end{aligned}
\tag{3}
$$

For a Euler-Bernoulli beam element in 2D,

$$
\begin{aligned}
U_{Continuum} &= \frac{V}{2}\gamma_{ij}C_{ijkm}\gamma_{km} + \frac{V}{2}\kappa_i D_{ij}\kappa_j \\
C_{ijkm} &= \sum_{b=1}^{N_b} n_i.n_k\left(n_j.n_m.(R)' + n_j.n_m.(R)''\right) \\
D_{ij} &= \sum_{b=1}^{N_b} n_i.n_j.S'
\end{aligned}
\tag{4}
$$

After the regularization of the lattice model and with minimization of the potential energy of the system, the load and displacements in each time step are determined. The bi-linear softening scheme is also implemented to model the quasi-brittle material behavior which is found in different geomaterial [20].

$$
\begin{aligned}
U_{Strain}(x) = U_{Axial}(x) + U_{Shear}(x) + U_{Moment}(x) = \frac{1}{2}\int_0^L \left(\frac{f_x(x)^2}{EA} + \frac{f_y(x)^2}{GA} + \frac{M(x)^2}{EI}\right).dx \\
E_s = \frac{f_t}{\varepsilon_f - \varepsilon_t}\left(\frac{\varepsilon_f}{\varepsilon} - 1\right)
\end{aligned}
\tag{5}
$$

3.2.3. Hydro-mechanical lattice model

The existing hydro-mechanical lattice models are based on the assumption of dual lattice network, where the mechanical lattice elements transfer the mechanical loads between two nodes and hydraulic conduct elements mostly perpendicular to the mechanical elements transfer the hydraulic and gas flow between conduct nodes [16, 17]. The implemented hydro mechanical lattice model is based on the mass conservation of fluids in the continuum.

$$
\begin{aligned}
m^{t+1} &= m^t + \Delta m \\
m^{t_0} &= \mathrm{Sr}^{t_0} V_{cavity} \rho_f \left(1 + \frac{P^{t_0}}{K_f}\right) \\
\Delta m_{ij} &= f\left(Sr\right).\frac{P_j - P_i - \rho_f g\left(y_j - y_i\right)}{R_a}.\Delta t
\end{aligned}
\tag{6}
$$

According to the finite-discrete element method (FDEM) [27], the physical and artificial cavities in a domain are defined. Each conduct node represents an artificial cavity connected through conductive elements, where the hydraulic conductivity is governed based on parallel plate flow cubic flow rules.

$$
\begin{aligned}
R_a &= \frac{12\nu_f}{a^3} L^{'} \\
R_a &= 12\nu_f \int_{s_i}^{s_j} \frac{1}{a\left(s^3\right)}\, ds = \frac{6\nu_f (a_j + a_i)}{\left(a_i a_j\right)^2} L^{'}
\end{aligned}
\tag{7}
$$

When an artificial cavity is saturated, the amount of excessive fluid mass flowing inside the cavity will result in hydraulic pressure, which will be then transformed into the mechanical mode. If the cavity is not saturated, then the hydraulic pressure is equal to zero.

$$
P^t = P^{t-1} + K_f \frac{\Delta m}{\rho_f V_{cavity}^t} \qquad if \quad \mathrm{Sr}^t = 1 \tag{8}
$$

With the implementation of measured pore pressures into the mechanical lattice nodes, the pore pressure diffusion and the change of hydraulic conductivity with crack opening are simulated. Both the pressure or flow rate controlled scheme can be implemented in this model.

3.3. Variational phase-field model

Phase-field models have become one of the standard approaches to the simulation of fracturing recently. The approach currently accepted as a variational phase-field model was first introduced by [8] as a regularized model of Francfort and Marigo energy functional [14]. Since this inception, the approach has been further studied for brittle and cohesive [9, 18, 4, 24, 47, 35, 48, 3, 29, 49, 45, 39] including advanced numerical solution schemes [15, 13]. Lately, its application ranges from ductile fracturing [3, 31, 25, 2] to fatigue [1, 44], desiccation fracture [30, 12], and dynamic fracturing [10, 7, 19, 43, 26].

3.3.1. Variational approach to hydraulic fracturing

Multiplying (1) by a test function $\boldsymbol{\phi} \in H^1(\Omega \setminus \Gamma)$ that vanishes on $\partial\Omega_{\mathrm{D}}$ and applying Green's formula yield:

$$
\int_{\Omega\setminus\Gamma_c} \mathbf{C}\left(\boldsymbol{\epsilon}(\mathbf{u}) - \frac{\alpha}{N\kappa} p_p \mathbf{I}\right) : \boldsymbol{\epsilon}(\boldsymbol{\phi})\, \mathrm{d}\Omega = \int_{\partial\Omega_{\mathrm{N}}^{\mathrm{m}}} \mathbf{t}\cdot\boldsymbol{\phi}\, \mathrm{d}\Gamma - \int_{\Gamma} p_f \left(\boldsymbol{\phi}\cdot\mathbf{n}_{\Gamma}\right)\, \mathrm{d}\Gamma,
$$

Then the weak form of the static equilibrium equations are written as

$$\mathcal{P} := \int_{\Omega\setminus\Gamma_{\mathrm{c}}} \psi\left(\mathbf{u}, p_p\right)\, \mathrm{d}\Omega - \int_{\partial\Omega_{\mathrm{N}}^{\mathrm{m}}} \mathbf{t}\cdot\mathbf{u}\, \mathrm{d}\Gamma + \int_{\Gamma} p_f\left(\mathbf{u}\cdot\mathbf{n}_{\Gamma}\right)\, \mathrm{d}\Gamma, \tag{9}$$

where

$$\psi\left(\mathbf{u}, p_p\right) := \frac{1}{2}\mathbf{C}\left(\boldsymbol{\epsilon}(\mathbf{u}) - \frac{\alpha}{N\kappa}p_p\mathbf{I}\right) : \left(\boldsymbol{\epsilon}(\mathbf{u}) - \frac{\alpha}{N\kappa}p_p\mathbf{I}\right) \tag{10}$$

is the poroelastic strain energy density [50].

Following the variational approach to brittle fracture proposed by Francfort and Marigo [14], we can define the total energy as

$$E = \mathcal{P} + G_{\mathrm{c}}\int_{\Gamma_{\mathrm{c}}} \mathrm{d}\Gamma. \tag{11}$$

In order to requlatize the discontinuities involved in Eq. (11), we follow the approximation proposed by Bourdin et al. [8, 11], which is now widely known as variational phase-field, and with the introduciton of the phase-field variable d, we obtain

$$E(\mathbf{u}, d; p) = \int_{\Omega}(1-d)^2\psi(\mathbf{u})\,\mathrm{d}\Omega - \int_{\partial\Omega_{\mathrm{N}}^{\mathrm{m}}}\mathbf{t}\cdot\mathbf{u}\,\mathrm{d}\Gamma + \frac{G_{\mathrm{c}}}{4c_w}\int_{\Omega}\left(\frac{w(d)}{\ell} + \ell\left|\nabla d\right|^2\right)\,\mathrm{d}\Omega + \int_{\Omega} p_f\mathbf{u}\cdot\nabla d\,\mathrm{d}\Omega. \tag{12}$$

where d takes 0 when undamaged and 1 for a fully damaged state, c_w is a normalization parameter defined as $c_w := \int_0^1 \sqrt{w(s)}\mathrm{d}s$. Various possible forms of the dissipative energy function $w(d)$ have been proposed [8, 24, 32, 7, 23] and in this study a linear form $w(d) = d$ is employed as in [50, 45]. The originally proposed energy functional (12) supports a contribution to the damage development from the entire strain energy ψ. However, this translates into an identical behaviour of the material under either in tension and compression and can also result in over penetration of the crack [4]. In order to circumvent such behavior, the strain energy is normally split into the part that drives the damage ψ^+ and the remaining ψ^- [32] as:

$$E(\mathbf{u}, d; p) = \int_{\Omega}(1-d)^2\psi^+(\mathbf{u}) + \psi^-(\mathbf{u})\,\mathrm{d}\Omega - \int_{\partial_{\mathrm{N}}\Omega}\mathbf{t}\cdot\mathbf{u}\,\mathrm{d}\Gamma + \frac{3G_{\mathrm{c}}}{8}\int_{\Omega}\left(\frac{d}{\ell} + \ell\left|\nabla d\right|^2\right)\,\mathrm{d}\Omega + \int_{\Omega} p_f\mathbf{u}\cdot\nabla d\,\mathrm{d}\Omega. \tag{13}$$

Several approaches for this split are available but this study employs the model known as spectral split [4] where the strain energies are split based on the sign of the principle strain, because it is able to provide a high contrast in the compressive-tensile strength ratio typically required in rocks [26]. With this split, the strain tensor is decomposed as:

$$\boldsymbol{\epsilon} = \epsilon_i\mathbf{M}_i \quad \text{with} \quad \mathbf{M}_i = \mathbf{n}_{(i)}\otimes\mathbf{n}_{(i)} \tag{14}$$

where $\mathbf{e}_{(i)}$ are the eigenvectors of the strain tensor and parentheses around an index indicate that no sum is taken. Then the strain energies are defiled as:

$$\psi^{\pm} = \frac{\lambda}{2}\left(\langle\epsilon_1 + \epsilon_2 + \epsilon_3\rangle^{\pm}\right)^2 + \mu\left[\left(\langle\epsilon_1\rangle^{\pm}\right)^2 + \left(\langle\epsilon_2\rangle^{\pm}\right)^2 + \left(\langle\epsilon_3\rangle^{\pm}\right)^2\right]. \tag{15}$$

3.3.2. Numerical implementation

In the variational phase-field model development in this study, leak-off to the rock mass is neglected given the ultra-tight permeability of rock salt. Therefore, p_p is constant and can be

regarded as $p_p = 0$ and $p'_f = p_f - p_p$ in the model. However, for the sake of conciseness, notation of $p'_f = p$ is adapted hereafter. Another simplification made is that p is spatially constant provided that the pressure loss within the crack is negligible. Then Eq. (12) is solved by the alternate minimization or staggered scheme with respect to the displacement $\mathbf{u}$ and the damage d with a constraint of prescribed time-evolving fluid volume which must be equal to the crack volume i.e. $V_{\text{inj}} = V_{\text{crack}} (= \int_\Omega \mathbf{u} \cdot \nabla d \, \mathrm{d}\Omega)$, see [51]. Thus, the minimisation problem can be stated as

$$(\mathbf{u}, d; p)^* = \quad \arg\min E(\mathbf{u}, d; p) \quad . \qquad \begin{cases} \mathbf{u} \in H^1 \\ d \in H^1, d^t \subset d^{t+\Delta t} \end{cases} \tag{16}$$

with the constrain of:

$$V_{\text{inj}} = \int_\Omega \mathbf{u} \cdot \nabla d \, \mathrm{d}\Omega \tag{17}$$

The first variation of the energy functional with respect to $\mathbf{u}$ is given by

$$\begin{aligned} \delta E(\mathbf{u}, d, p; \delta \mathbf{u}) = \frac{1}{2} \int_\Omega \boldsymbol{\epsilon}(\delta \mathbf{u}) : \left\{ (1-d)^2 \boldsymbol{\mathcal{C}}^+ + \boldsymbol{\mathcal{C}}^- \right\} : \boldsymbol{\epsilon}(\mathbf{u}) \, \mathrm{d}\Omega \\ - \int_{\partial_{\mathrm{N}}\Omega} \mathbf{t} \cdot \delta \mathbf{u} \, \mathrm{d}\Gamma - \int_\Omega \mathbf{f} \cdot \delta \tilde{\mathbf{u}} \, \mathrm{d}\Omega + \int_\Omega p \delta \mathbf{u} \cdot \nabla d \, \mathrm{d}\Omega, \end{aligned} \tag{18}$$

where $\boldsymbol{\mathcal{C}}^\pm$ is the tangent stiffness tenser defined as

$$\boldsymbol{\mathcal{C}}^\pm = \frac{\partial}{\partial \boldsymbol{\epsilon}} \left(\frac{\partial \psi^\pm}{\partial \boldsymbol{\epsilon}} \right). \tag{19}$$

The first variation of the energy functional with respect to d is given as

$$\begin{aligned} \delta E(\mathbf{u}, d, p; \delta d) = - \int_\Omega d \delta d \boldsymbol{\mathcal{C}}^+ (\, \boldsymbol{\epsilon}(\mathbf{u})) : \, \boldsymbol{\epsilon}(\mathbf{u}) \, \mathrm{d}\Omega \\ + \frac{3 G_{\mathrm{c}}}{8} \int_\Omega \left(\frac{\delta d}{\ell} + 2 \ell \nabla d \cdot \nabla \delta d \right) \mathrm{d}\Omega + \int_\Omega p \mathbf{u} \cdot \nabla \delta d \, \mathrm{d}\Omega, \end{aligned} \tag{20}$$

In our analysis, as the material is under the external loading, the force equlibrium is decomposed into following two problems:

$$\begin{cases} \nabla \cdot \boldsymbol{\sigma}(\mathbf{u}_p) = \mathbf{0} & \text{in } \Omega \setminus \Gamma_{\mathrm{c}}, \\ \boldsymbol{\sigma} \cdot \mathbf{n} = \mathbf{0} & \text{on } \partial\Omega_{\mathrm{N}_p}, \\ \mathbf{u}_p = \mathbf{u}_{p0} & \text{on } \partial\Omega_{\mathrm{D}_p}, \\ \boldsymbol{\sigma}^\pm \cdot \mathbf{n}_{\Gamma^\pm} = -\mathbf{n}_{\Gamma^\pm} & \text{on } \Gamma_{\mathrm{c}}^\pm. \end{cases} \tag{21}$$

and

$$\begin{cases} \nabla \cdot \boldsymbol{\sigma}(\mathbf{u}_s) = \mathbf{0} & \text{in } \Omega \setminus \Gamma_{\mathrm{c}}, \\ \boldsymbol{\sigma} \cdot \mathbf{n} = \mathbf{t} & \text{on } \partial\Omega_{\mathrm{N}_s}, \\ \mathbf{u}_s = \mathbf{u}_{s0} & \text{on } \partial\Omega_{\mathrm{D}_s}, \\ \boldsymbol{\sigma}^\pm \cdot \mathbf{n}_{\Gamma^\pm} = \mathbf{0} & \text{on } \Gamma_{\mathrm{c}}^\pm. \end{cases} \tag{22}$$

Then the solution to (1) is obtained from $\mathbf{u} = \mathbf{u}_s + p\mathbf{u}_p$. Substituting into Eq. (17) yields

$$V_{\text{inj}} = \int_\Omega \mathbf{u}_s \cdot \nabla d \, \mathrm{d}\Omega + p \int_\Omega \mathbf{u}_p \cdot \nabla d \, \mathrm{d}\Omega. \tag{23}$$

Thus the fluid pressure is obtained as

$$p = \frac{V_{\text{inj}} - V_s}{V_p}, \tag{24}$$

where

$$V_s = \int_\Omega \mathbf{u}_s \cdot \nabla d \, \mathrm{d}\Omega, \tag{25}$$

and

$$V_p = \int_\Omega \mathbf{u}_p \cdot \nabla d \, \mathrm{d}\Omega. \tag{26}$$

Algorithm 1 Incorporation of the volume constraint in the phase-field model.

repeat
  Update the injected volume, $V_{\text{inj}}(t_n + \Delta t)$
  repeat
    Solve for $\mathbf{u}_p$
    Solve for $\mathbf{u}_s$
    Calculate pressure, $p = \frac{V_{\text{inj}} - V_s}{V_p}$
    Update the displacement, $\mathbf{u} = \mathbf{u}_s + p\mathbf{u}_p$
    Solve for d
  until $\|d - d_n\| < 10^{-4}$
until $V < V_{\text{final}}$

4. Results and discussion

4.1. LEM result

The dual lattice element method is implemented to simulate the hydraulic fracture. 5 depicts the cross-section of simulated setup using LEM. The total number of lattice (mechanical) and conduct (hydraulic) elements are around 60000 and 400000. The experimental setup shown in **??** is implemented into dual LEM and the developed fractures and flow path are shown in 5(a) and 5(b). Similarly, the second stress configuration, see **??**, is simulated and the fracture surfaces as well as flow paths are shown in 6(a) and 6(b), respectively.

Mechanical properties of saltstone used for simulation are listed in 1.

4.2. VPF result

A computational domain for the variational phase-field model is depicted in Fig 7. Relying on the symmetry of the domain, 1/4 of the domain was simulated. The whole domain was discretized with first-order tetrahedral elements. The total element count is 27,917,126 with 5,432,325 nodes. and simulated crack development in Fig 8.

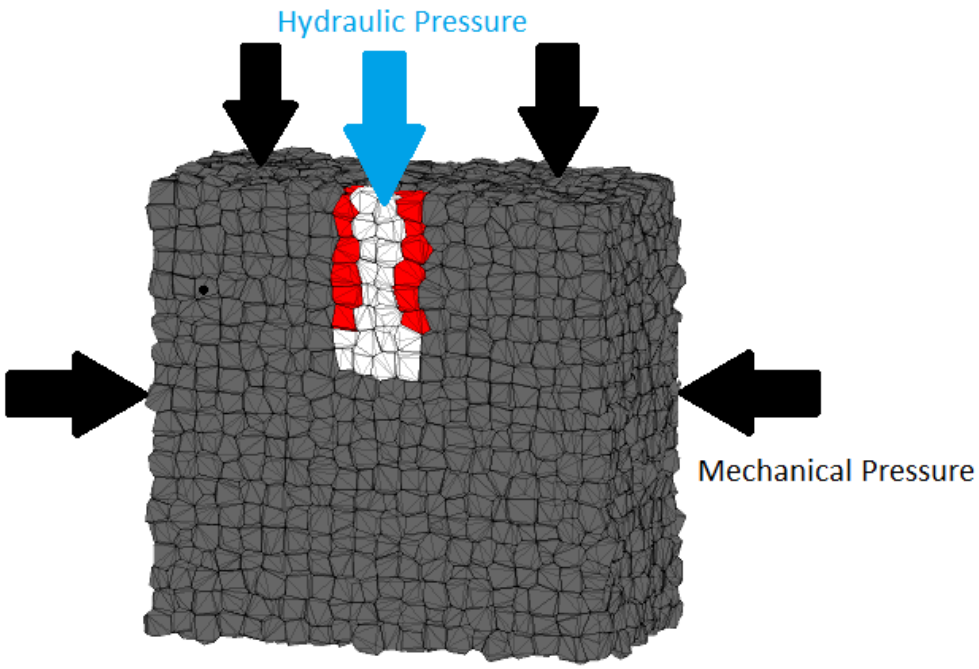

Figure 4: The ME2 fist stress configuration in dual LEM.

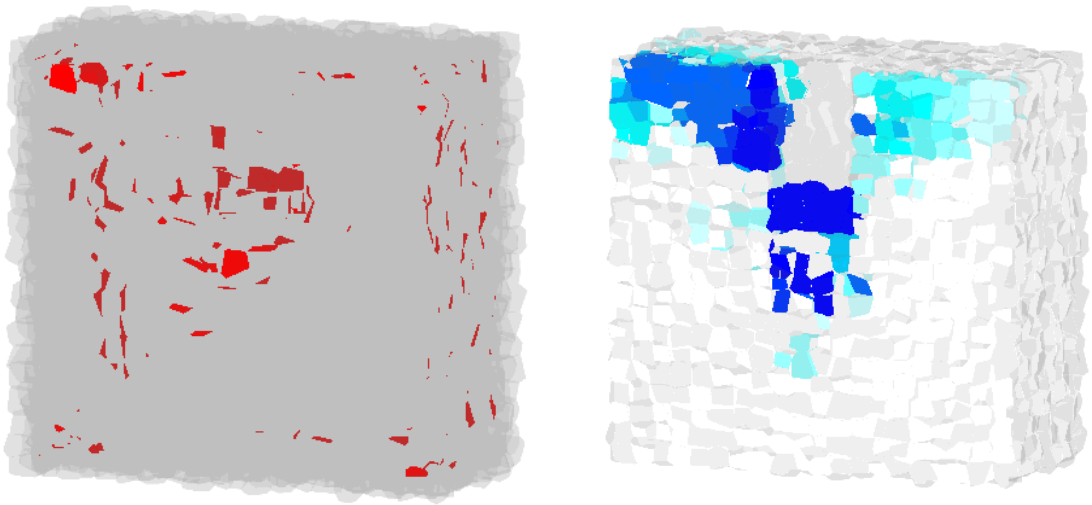

(a) The developed fractures shown with red surfaces in Z-X cross-section plane (LEM).

(b) The developed flow path shown with blue surfaces in Z-X cross-section plane (LEM)

Figure 5: The simulation of fluid driven percolation shown in **??**

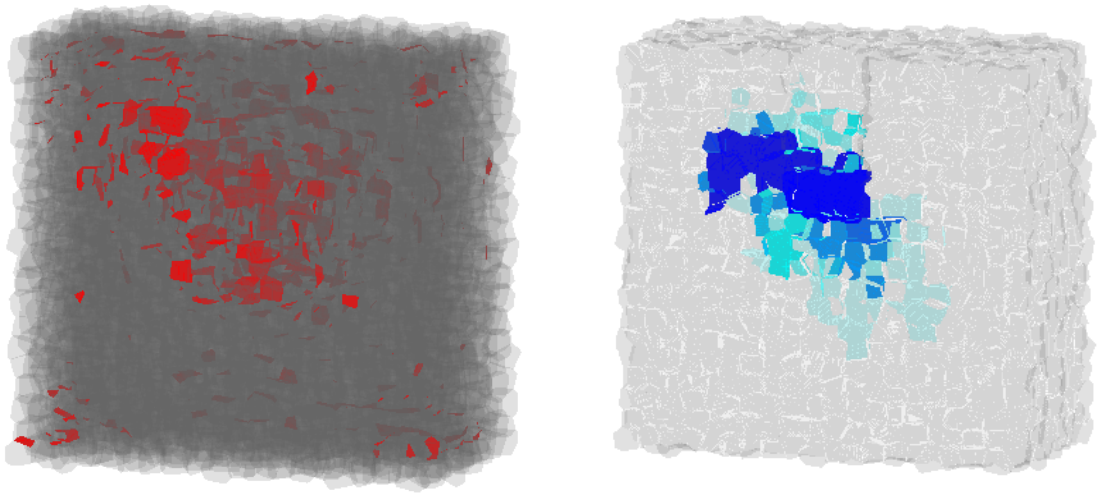

(a) The developed fractures shown with red surfaces in Z-X cross-section plane (LEM)

(b) The developed flow path shown with blue surfaces in Z-X cross-section plane (LEM)

Figure 6: The simulation of fluid driven percolation shown in **??**

Table 1: Mechanical properties

Parameter	**Value**
K	16.7 GPa
G	10 GPa
G_c	100 Pa m

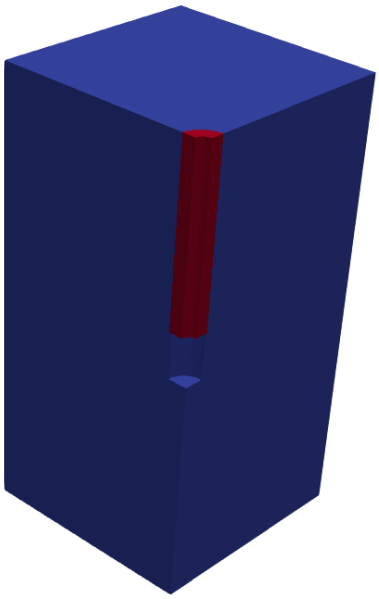

Figure 7: A computational domain for the variational phase-field model.

5. Conclusions

Acknowledgements

The authors gratefully acknowledge the funding provided by the German Federal Ministry of Education and Research (BMBF) for the GeomInt project, Grant Number 03G0866A, as well as the support of the Project Management Jülich (PtJ).

[1] R. Alessi, M. Ambati, T. Gerasimov, S. Vidoli, and L. De Lorenzis. *Comparison of Phase-Field Models of Fracture Coupled with Plasticity*, pages 1–21. Springer International Publishing, Cham, 2018.

[2] R. Alessi, J. J. Marigo, C. Maurini, and S. Vidoli. Coupling damage and plasticity for a phase-field regularisation of brittle, cohesive and ductile fracture: One-dimensional examples. *International Journal of Mechanical Sciences*, pages 1–18, 2017.

[3] M. Ambati, T. Gerasimov, and L. De Lorenzis. Phase-field modeling of ductile fracture. *Computational Mechanics*, 55(5):1017–1040, 2015.

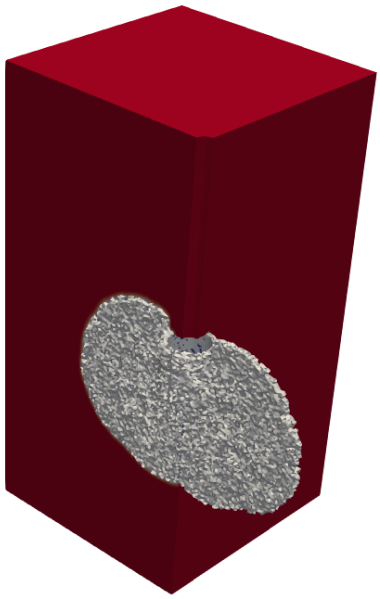

Figure 8: Simulated crack propagation from the variational phase-field model.

[4] Hanen Amor, Jean-jacques Marigo, and Corrado Maurini. Regularized formulation of the variational brittle fracture with unilateral contact: numerical experiments. *Journal of Mechanics and Physics of Solids*, 57(8):1209–1229, 2009.

[5] E M Anderson. The dynamics of faulting. *Transactions of the Edinburgh Geological Society*, 8(3):387–402, 1905.

[6] J.E. Bolander and S. Saito. Fracture analyses using spring networks with random geometry. *Engineering Fracture Mechanics*, 6:1569–1591, 1998.

[7] M.J. Borden, C.V. Verhoosel, M.A. Scott, T.J.R. Hughes, and C.M. Landis. A phase-field description of dynamic brittle fracture. *Computer Methods in Applied Mechanics and Engineering*, 217-220:77–95, 2012.

[8] B. Bourdin, G.A. Francfort, and J.-J. Marigo. Numerical experiments in revisited brittle fracture. *J. Mech. and Phys. of Solids*, 48(4):797–826, 2000.

[9] B. Bourdin, G.A. Francfort, and J.-J. Marigo. The variational approach to fracture. *Journal of Elasticity*, 91(1-3):5–148, 2008.

[10] B. Bourdin, C.J. Larsen, and C.L. Richardson. A time-discrete model for dynamic fracture based on crack regularization. *International Journal of Fracture*, 168(2):133–143, 2011.

[11] Blaise Bourdin, Chukwudi P. Chukwudozie, and Keita Yoshioka. A Variational Approach to the Numerical Simulation of Hydraulic Fracturing. In *the 2012 SPE Annual Technical Conference and Exhibition*, 2012.

[12] T. Cajuhi, L. Sanavia, and Laura De Lorenzis. Phase-field modeling of fracture in variably saturated porous media. *Computational Mechanics*, pages 1–20, 2017.

[13] P. Farrell and C. Maurini. Linear and nonlinear solvers for variational phase-field models of brittle fracture. *International Journal for Numerical Methods in Engineering*, 109(5):648–667, 2017.

[14] G.A. Francfort and J.-J Marigo. Revisiting brittle fracture as an energy minimization problem. *J. Mech. and Phys. of Solids*, 46(8):1319–1342, 1998.

[15] T. Gerasimov and L. De Lorenzis. A line search assisted monolithic approach for phase-field computing of brittle fracture. *Computer Methods in Applied Mechanics and Engineering*, 312:276 – 303, 2016. Phase Field Approaches to Fracture.

[16] P. Grassl. A lattice approach to model flow in cracked concrete. *Cement & Concrete Composites*, 31:454460, 2009.

[17] P. Grassl, C. Fahy, D. Gallipoli, and J. Bolander. A lattice model for liquid transport in cracked unsaturated heterogeneous porous materials. *VIII International Conference on Fracture Mechanics of Concrete and Concrete Structures*, 2013.

[18] V. Hakim and A. Karma. Laws of crack motion and phase-field models of fracture. *Journal of the Mechanics and Physics of Solids*, 57(2):342–368, 2009.

[19] M. Hofacker and C. Miehe. Continuum phase field modeling of dynamic fracture: Variational principles and staggered FE implementation. *International Journal of Fracture*, 178(1-2):113–129, 2012.

[20] R. Ince, A. Arslan, and B.L. Karihaloo. Lattice modelling of size effect in concrete strength. *Engineering Fracture Mechanics*, 70:23072320, 2003.

[21] W.P. Kamlot. *Habilitationsschrift: Gebirgsmechanische Bewertung der geologischen Barrierefunktion des Hauptanhydrits in einem Salzbergwerk*. des Instituts fr Geotechnik der Technischen Universitt Bergakademie Freiberg, 2009.

[22] B.L. Karihaloo, P.F. Shao, and Q.Z. Xiao. Lattice modelling of the failure of particle composites. *Engineering Fracture Mechanics*, 70:23852406, 2003.

[23] Markus Klinsmann, Daniele Rosato, Marc Kamlah, and Robert M. McMeeking. An assessment of the phase field formulation for crack growth. *Computer Methods in Applied Mechanics and Engineering*, 294(Supplement C):313 – 330, 2015.

[24] C. Kuhn and R. Müller. A continuum phase field model for fracture. *Engineering Fracture Mechanics*, 77(18):3625–3634, 2010.

[25] C. Kuhn, T. Noll, and R. Müller. On phase field modeling of ductile fracture. *GAMM Mitteilungen*, 39(1):35–54, 2016.

[26] T. Li, J.-J. Marigo, D. Guilbaud, and S. Potapov. Gradient damage modeling of brittle fracture in an explicit dynamic context. *International Journal for Numerical Methods in Engineering*, 00(March):1–25, 2016.

[27] A. Lisjak, P. Kaifosh, L. Hea, B.S.A. Tatone, O.K. Mahabadi, and G. Grasselli. A 2d, fully-coupled, hydro-mechanical, fdem formulation for modelling fracturing processes in discontinuous, porous rock masses. *Computers and Geotechnics*, 81:118, 2017.

[28] J.X. Liu, S.C. Deng, J. Zhang, and N.G Liang. Lattice type of fracture model for concrete. *Theoretical and Applied Fracture Mechanics*, 48:269284, 2007.

[29] J.-J. Marigo, C. Maurini, and K. Pham. An overview of the modelling of fracture by gradient damage models. *Meccanica*, 51(12):3107–3128, 2016.

[30] C. Maurini, B. Bourdin, G. Gauthier, and V. Lazarus. Crack patterns obtained by unidirectional drying of a colloidal suspension in a capillary tube: Experiments and numerical simulations using a two-dimensional variational approach. *International Journal of Fracture*, 184(1-2):75–91, 2013.

[31] C. Miehe, M. Hofacker, L. M. Schänzel, and F. Aldakheel. Phase field modeling of fracture in multi-physics problems. Part II. Coupled brittle-to-ductile failure criteria and crack propagation in thermo-elastic-plastic solids. *Computer Methods in Applied Mechanics and Engineering*, 294:486–522, 2015.

[32] C. Miehe, F. Welschinger, and M. Hofacker. Thermodynamically consistent phase-field models of fracture: Variational principles and multi-field fe implementations. *International Journal for Numerical Methods in Engineering*, 83(10):1273–1311, 2010.

[33] C. Moukarzel and H. J. Herrmann. A vectorizable random lattice. *J. Stat. Phys.*, 68:911923, 1992.

[34] M. Ostoja-Starzewski. Lattice models in micromechanics. *Applied mechanics*, 55(1):35–60, 2002.

[35] K. Pham, H. Amor, J.-J. Marigo, and C. Maurini. Gradient damage models and their use to approximate brittle fracture. *Int. J. Damage Mech.*, 20(4, SI):618–652, 2011.

[36] E.P. Prado and J.G.M. van Mier. Effect of particle structure on mode i fracture process in concrete. *Engineering Fracture Mechanics*, 70:17931807, 2003.

[37] Z. H. Rizvi, M. Nikolic, and F. Wuttke. Lattice element method for simulations of failure in bio-cemented sands. *Granular Matter*, 21(18), 2019.

[38] Z.H. Rizvi, D. Shrestha, A.S. Sattari, and F. Wuttke. Numerical modelling of effective thermal conductivity for modified geomaterial using lattice element method. *Heat Mass Transf*, 54(2):483499, 2018.

[39] J.M. Sargado, E. Keilegavlen, I. Berre, and J.M. Nordbotten. High-accuracy phase-field models for brittle fracture based on a new family of degradation functions. *Journal of the Mechanics and Physics of Solids*, 111:458 – 489, 2018.

[40] A. S. Sattari, H. B. Motra, Z. H. Rizvi, and F. Wuttke. Dynamic analysis by lattice element method simulation. *Proceedings of China-Europe Conference on Geotechnical Engineering*, pages 405–409, 2018.

[41] A. S. Sattari, H. B. Motra, Z. H. Rizvi, and F. Wuttke. A new lattice element method (lem) with integrated interface elements for determining the effective thermal conductivity of rock solids under thermo-mechanical processes. *International Symposium on Energy Geotechnics (SEG), Energy Geotechnics*, pages 266–275, 2018.

[42] A.S. Sattari, Z.H. Rizvi, H.B. Motra, and F. Wuttke. Meso-scale modeling of heat transport in a heterogeneous cemented geomaterial by lattice element method. *Granular Matter*, 19(66), 2017.

[43] A. Schlüter, A. Willenbücher, C. Kuhn, and R. Müller. Phase field approximation of dynamic brittle fracture. *Computational Mechanics*, 54(5):1141–1161, 2014.

[44] M. Seiler, P. Hantschke, A. Brosius, and M. Kästner. A numerically efficient phase-field model for fatigue fracture - 1D analysis. *Pamm*, 18(1):e201800207, 2018.

[45] E. Tanné, T. Li, B. Bourdin, J-J. Marigo, and C. Maurini. Crack nucleation in variational phase-field models of brittle fracture. *J. Mech. Phys. Solids*, 110:80–99, 2018.

[46] J.G.M. van Mier, M.R.A. van Vliet, and K. Wang Tai. Fracture mechanisms in particle composites: statistical aspects in lattice type analysis. *Mechanics of Materials*, 34, 2002.

[47] C.V. Verhoosel and R. de Borst. A phase-field model for cohesive fracture. *International Journal for Numerical Methods in Engineering*, 00:1–20, 2010.

[48] Julien Vignollet, Stefan May, René de Borst, and Clemens V. Verhoosel. Phase-field models for brittle and cohesive fracture. *Meccanica*, 49(11):2587–2601, 2014.

[49] J.-Y. Wu. A unified phase-field theory for the mechanics of damage and quasi-brittle failure. *Journal of the Mechanics and Physics of Solids*, 103:72 – 99, 2017.

[50] K. Yoshioka and B. Bourdin. A variational hydraulic fracturing model coupled to a reservoir simulator. *Int. J. Rock Mech. Min.*, 88:137–150, 2016.

[51] K. Yoshioka, F. Parisio, D. Naumov, R. Lu, O. Kolditz, and T. Nagel. Comparative verification of discrete and smeared numerical approaches for the simulation of hydraulic fracturing. *GEM - International Journal on Geomathematics*, 10(1), 2019.